





Direct observation of mass-dependent collisionless energy transfer via Landau and transit-time damping

journal or publication title	Communications Physics
volume	5
number	228
year	2022-09-28
NAIS	13344
URL	http://hdl.handle.net/10655/00013509

doi: <https://doi.org/10.1038/s42005-022-01008-9>



Direct observation of mass-dependent collisionless energy transfer via Landau and transit-time damping

Katsumi Ida ^{1,2}✉, Tatsuya Kobayashi^{1,2}, Mikiro Yoshinuma¹, Kenichi Nagaoka ^{1,3}, Kunihiro Ogawa ^{1,2}, Tokihiko Tokuzawa^{1,2}, Hideo Nuga¹ & Yuto Katoh ⁴

The energy transfer from wave to particle occurs in collisionless plasma through the interaction between particle and wave, associated with the deformation of ion velocity space from Maxwell-Boltzmann distribution. Here we show the direct observation of mass-dependent collisionless energy transfer via Landau and transit-time damping in a laboratory plasma. The Landau and transit-time damping are confirmed by the bipolar velocity-space signature of the ion velocity distribution function, measured by fast charge exchange spectroscopy with a time resolution less than ion-ion collision time. The excellent agreement between the resonant phase velocity evaluated from the bipolar velocity-space signature and the wave's phase velocity, estimated from the frequency of the magnetohydrodynamics oscillation measured with the plasma displacement is clear evidence for the Landau damping. The energy transfer from solitary wave to fully ionized carbon impurity ions is larger than that of bulk ions 2-3 times due to heavier mass.

¹National Institute for Fusion Science, National Institutes of Natural Sciences, Toki, Gifu 509-5292, Japan. ²The Graduate University for Advanced Studies, SOKENDAI, Toki, Gifu 509-5292, Japan. ³Graduate School of Science, Nagoya University, Nagoya, Aichi 464-8602, Japan. ⁴Graduate School of Science, Tohoku University, Sendai, Miyagi 980-8578, Japan. ✉email: ida.katsumi@nifs.ac.jp

Landau damping and transit-time damping are well-known resonant wave-particle interactions in which energy is transferred from the wave to ions or electrons in the plasma^{1–7}. Both Landau damping and transit-time damping result in a net transfer of energy from the wave to the particles and consequent damping of the wave. In this experiment, the difference between Landau damping and transit-time damping is characterized by the damping rate of the wave. In the Landau damping, the damping rate is lower than the oscillation frequency, and several cycles of the wave appear before it damps. The wave-particle interactions occur at a single resonant frequency. However, the damping rate is higher than the oscillation frequency and wave damps within one cycle. Then the Fourier component of the wave has a broad spectrum, and wave-particle interactions occur at a broadband resonant frequency. The Landau damping has been observed for ion-acoustic waves⁸, plasma waves^{9–11}, solitary wave¹², and Alfvén waves¹³ in laboratory plasma (linear plasma device) and for kinetic Alfvén waves in heliospheric plasmas^{14–16} and magnetosheath plasma^{17,18}. In the Landau and transit-time damping process, the particles initially moving at velocities slightly slower than the phase velocity of the wave, gain energy from the wave, while the particles initially moving at velocities slightly faster than the phase velocity, lose energy to the wave. Because the number of particles with velocities smaller than the wave phase velocity is greater than those with velocities larger than the wave phase velocity in the Maxwell-Boltzmann distribution, this process results in a decay of the wave amplitude and an increase in the kinetic energy of particles. In the previous experiment in the linear plasma device, the wave was excited externally, and the damping distance of the wave amplitude was measured. Then the Landau damping process was confirmed by comparing the damping rate of the wave to the prediction in theory^{8–11}.

Because Landau and transit-time damping are collisionless interactions between particles and waves, the energy transfer is associated with a distortion of the ion velocity distribution function from the Maxwell-Boltzmann distribution. Therefore, the measurement of deformation of the velocity distribution is critical for the identification of Landau and transit-time damping¹⁹. This non-thermal deformation is characterized by the simultaneous increase/decrease of particles with velocities larger/smaller than the resonant phase velocity, called a bipolar velocity-space signature^{13,18}. Therefore, observation of this bipolar velocity-space signature is clear evidence for the Landau damping and the inverse Landau damping, and the sign of the bipolar signature is the opposite of these two processes. The number of particles with velocities larger than the resonant phase velocity increases (energy transfer from the wave to the particle) for the Landau/transit-time damping, while the number of particles with velocities larger than the resonant phase velocity (Methods) decreases (energy transfer from the particle to the wave) for the inverse Landau/transit-time damping. The energy transfer between charged particles and the magnetohydrodynamics (MHD) mode occurs through the magnetic (grad-B and curvature) drifts and the perpendicular electric field²⁰. Magnetohydrodynamic hybrid simulation, including the kinetic effect, predicts Landau damping and inverse Landau damping for acoustic modes and MHD modes^{21–24}. Here, we present the mass-dependent collisionless energy transfer from solitary wave to multi-species plasma, based on direct measurement of velocity space on fully ionized carbon impurity ions, C⁶⁺, using fast charge exchange spectroscopy (Methods) with a time resolution (10 kHz for carbon impurity ions and 2 kHz for bulk ions) less than ion-ion collision time ($\sim 10^{-3}$ sec for carbon impurity ions and $\sim 10^{-2}$ sec for bulk ions in this plasma).

Results

Characteristics of the MHD event. This experiment was performed in a magnetically confined toroidal plasma heated by

neutral beams (NBs) in the Large Helical Device (LHD) (Methods). The total plasma β (the ratio of the plasma pressure to the magnetic pressure) is $\sim 1\%$. The beam pressure is comparable to the bulk plasma pressure. When the pressure of trapped energetic ions injected by deuterium neutral beams exceeds a critical value, MHD instability with transient large-amplitude magnetic perturbation occurs, which is called an MHD burst^{25–31} (Methods). The beam pressure is the energy source for exciting waves in the MHD burst. In the region where the instability is excited (at $r_{\text{eff}}/a_{99} = 0.79$), the electron density is $0.8 \times 10^{19} \text{ m}^{-3}$, and the electron and the ion temperatures are 2.5 and 2 keV, respectively. Here r_{eff} is the effective minor radius of the plasma, and a_{99} is the effective minor radius in which 99% of the plasma kinetic energy is confined. The amplitude of the magnetic field perturbation during the MHD burst is measured with toroidal magnetic probe arrays³² installed inside the vacuum vessel of the LHD.

The Landau damping and transit-time damping are observed in the plasma when the MHD burst with large amplitude occurs with deuterium beam injection perpendicular to the magnetic field. Figure 1a, c, e, g, i shows the characteristics of the discharge for transit-time, while Fig. 1b, d, f, h, j shows the features of the shot for Landau damping. The amount of deuterium beam pressure is monitored by the neutron flux (Methods) measured with a scintillation detector³³. In this experiment, we evaluate the behavior of beam ions through the measurement of the neutron flux from the D-D reaction. The TASK/FP code³⁴ estimates that the beam-thermal reaction contributes 94% of neutron flux. Therefore, the drop in the neutron emission rate indicates a rapid decrease of deuterium beam pressure perpendicular to the magnetic field and is called a trapped particle. The high radio frequency (RF) intensity, measured with an RF radiation probe³⁵, shows a sharp increase which is excited by the energetic ions at the plasma edge³⁶. The simultaneous decrease of neutron emission and RF intensity increase indicates an abrupt loss of trapped energetic ions associated with the MHD burst. As seen in Fig. 1c and d, the neutron flux suddenly drops by $\sim 30\%$ when the

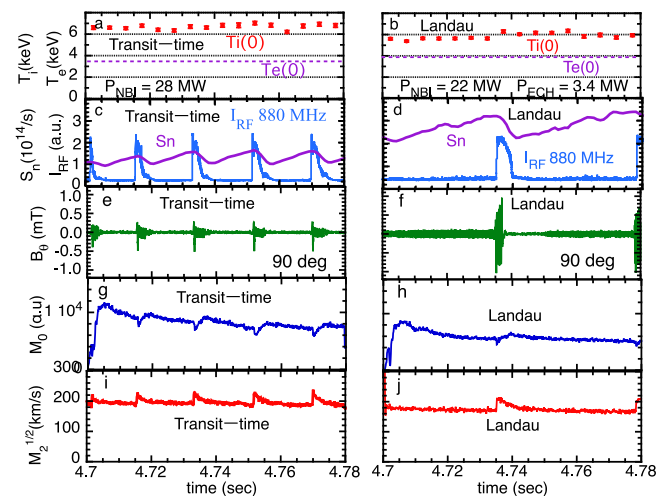


Fig. 1 Plasma discharges with transit-time damping and Landau damping.

Time evolution of **a**, **b** central electron temperature, $T_e(O)$, and ion temperature, $T_i(O)$, **c**, **d** neutron emission rate, S_n (purple lines), and radio frequency (RF) intensity, I_{RF} (blue lines), measured by radio frequency (RF) radiation probe ($\phi = 121^\circ$), **e**, **f** magnetic field perturbation at $\phi = 198^\circ$, **g**, **h** Oth moment and **i**, **j** square root of 2nd moment of the ion velocity distributions in the discharge with **a**, **c**, **e**, **g**, **i** transit-time damping and **b**, **d**, **f**, **h**, **j** Landau damping (#165968 and #165862). The error bars in **a** and **b** are uncertainties of ion temperature measured from line broadening with charge exchange spectroscopy.

MHD burst occurs and gradually recovers after the disappearance of the MHD burst. Therefore, the longer interval further increases the pressure of the trapped energetic ions at the MHD burst, as indicated by the more significant neutron emission flux. The interval between MHD bursts is sensitive to the plasma parameter such as central ion and electron temperature and becomes longer when the ratio of ion to electron temperature decreases by applying electron cyclotron heating (ECH)³⁷.

The amplitude of the magnetic field perturbation during the MHD burst is ~ 0.5 mT for transit-time damping and is ~ 1 mT for Landau damping; those are much larger than the amplitude of the magnetic field oscillations observed between the MHD bursts (0.01–0.1 mT). This is because the amplitude of the magnetic field perturbation during the MHD burst becomes more substantial and more prolonged (up to 2 ms) for the Landau damping than the transit-time damping due to the increase of pressure of trapped energetic ions during the interval period. Moment analysis (Methods) is applied to the velocity distribution, measured by charge exchange spectroscopy, viewing the plasma toroidally. The energy gain of ions is evaluated by the increase in the M_0M_2 value of ion velocity distribution function, f , evaluated from the intensity of spectrum measured with charge exchange spectroscopy³⁸. As seen in Fig. 1i and j, the square root of the M_2 value of carbon impurity ions increases by 20%, while the M_0 value shows a negative spike for the transit-time damping but not for the Landau damping, associated with the onset of the MHD burst. The M_2 values gradually decay afterward, due to the collision between carbon impurity and bulk ions.

The MHD burst is triggered by the collapse of a tongue-shaped deformation, which occurs not at the resonant magnetic flux surface, the so-called rational surface, but the off-resonant magnetic flux surface^{27–29}. The unstable wave modes involved in the wave-particle interactions are different in the case of Landau and transit-time experiments. This post-cursor wave mode before the main event (collapse of a tongue-shaped deformation) is too weak to involve in the wave-particle interactions for the transit-time damping case but strong enough to affect the wave-particle interactions for the Landau damping case. In the case of Landau damping, both the solitary wave excited by the collapse of the tongue-shaped deformation and the post-cursor wave appearing after the main event contributes to the deformation of velocity distribution function via the wave-particle interactions. In this experiment, we applied ECH to increase the time interval between two MHD bursts and, more importantly, increase the amplitude of each MHD burst. The ECH can reduce the number of MHD bursts but not decrease the magnitude of MHD bursts if they occur. Therefore, the effect of ECH increases the threshold of the tongue-shaped deformation rather than stabilizing MHD instability. The ECH enhances the magnitude of the post-cursor wave mode, which is strong enough to cause wave-particle interactions and results in Landau damping.

Landau damping. Figure 2 shows an expanded view of the magnetic field perturbation and plasma displacement, measured by electron cyclotron emission (ECE)³⁹ at $r_{\text{eff}}/a_{99} = 0.83$ and skewness (M_3) of ion velocity distribution at $r_{\text{eff}}/a_{99} = 0.79$. Although there is a higher velocity component of ions, especially bulk ones, due to the slowing down of energetic particles injected by a neutral beam, this component is too small to be measured with charge exchange spectroscopy. In this paper, skewness is used as an indicator of the wave-particle interactions' impact on the deformation of ion velocity distribution. In order to increase the signal-to-noise ratio of the measurement, the conditional averaging technique (Methods) is applied to magnetic field

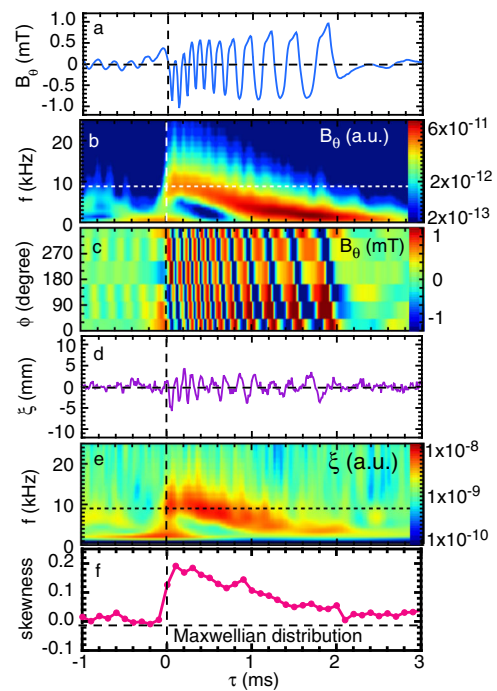


Fig. 2 Characteristics of Landau damping. Time evolution of **a** magnetic field perturbation, **b** frequency spectrum power of magnetic field perturbation, **c** contour of magnetic field perturbation, **d** plasma displacement at $r_{\text{eff}}/a_{99} = 0.83$ evaluated from perturbation of electron temperature, **e** frequency spectrum power of plasma displacement, and **f** skewness of ion velocity distribution function at $r_{\text{eff}}/a_{99} = 0.79$ with conditional averaging with respect to the collapse time of energetic ions, as indicated by the sharp increase in radio frequency (RF) intensity, plotted in Fig. 1d. (#164992, #165851, #165859, #165862, #165863, #165943, #165971, #165977).

perturbation, plasma displacement, and skewness of the ion velocity distribution function. Here, the sharp increase in radio frequency (RF) intensity, plotted in Fig. 1d, is used to reference the onset of the MHD burst. Both the magnetic field perturbation and the plasma displacement at $r_{\text{eff}}/a_{99} = 0.83$, show a feature of down-chirping from 9 to 2 kHz after the onset of the MHD burst. The initial mode frequency at the onset of the MHD burst is determined by a parallel precession of the resonant trapped energetic ions³¹. The contour of magnetic field perturbation at the toroidal angle and in time-space indicates that this magnetic field perturbation is a rotating mode in the toroidal direction (nearly parallel to the magnetic field) with a toroidal mode number $n = 1$. The skewness, M_3 value, is an excellent measure to quantify the distortion of the ion velocity distribution function from the Maxwell-Boltzmann distribution. Before the onset of the MHD burst, the skewness at $r_{\text{eff}}/a_{99} = 0.79$ is close to zero, which indicates that the ion velocity distribution function is Maxwell-Boltzmann distribution. However, the skewness jumps to 0.2 at the onset of the MHD burst within 0.1 ms, as seen in Fig. 2f. Then, the skewness gradually decreases during the down-chirping of the exciting wave in the plasma in 2 ms. The jump of skewness from zero to 0.2 indicates the rapid distortion of the ion velocity distribution function from Maxwell-Boltzmann distribution at the onset of an MHD burst.

It is well known that distortion of velocity function from Maxwell-Boltzmann distribution due to Landau damping has a so-called bipolar velocity-space signature. The bipolar velocity-space signature is characterized by an increase in the population of particles with velocities larger than the resonant phase velocity

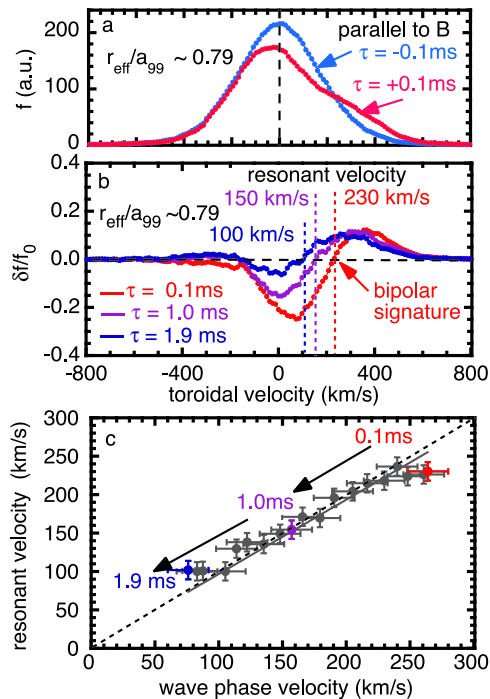


Fig. 3 Resonant velocity of Landau damping. **a** Distribution function of ion velocity at $r_{\text{eff}}/a_{99} = 0.79$ and at 0.1 ms before (blue circles) and after (red circles) the onset of MHD (magnetohydrodynamics) burst, **b** the difference of velocity distribution function between 0.1 ms before and 0.1 ms (red circles), 1.0 ms (purple circles), 1.9 ms (dark blue circles) after the onset of MHD burst. **c** relation between the phase velocity of wave evaluated from the frequency of plasma displacement plotted in Fig. 2e. The error bars of resonant velocity and wave phase velocity are uncertainties attributed to an evaluation of zero-cross velocity of bipolar signature and peak frequency of plasma displacement, respectively. (#164992, #165851, #165859, #165862, #165863, #165943, #165971, #165977).

and a decrease in the population of particles with velocities smaller than the resonant phase velocity. At the onset of the MHD burst, this bipolar velocity-space signature is clearly observed. Figure 3a shows the ion velocity distribution, measured with charge exchange spectroscopy at -0.1 ms before and 0.1 ms after the onset of the MHD burst, where the skewness value jumps from zero to 0.2 . The difference in ion velocity distribution between -0.1 ms (before the onset of the MHD burst) and 0.1 , 1.0 , 1.9 ms after the start of the MHD burst, plotted in Fig. 3b, shows the clear bipolar velocity-space signature. The distortion of velocity function from Maxwell-Boltzmann distribution with a bipolar velocity-space signature is observed only in the direction parallel to the magnetic field, not in the one perpendicular to it. This is consistent with the prediction of distortion of velocity function due to the Landau damping of the wave propagating in the direction parallel to the magnetic field. The bipolar velocity-space signature varies during the down-chirping wave excited in the plasma. The velocity for zero crossings in the bipolar signature corresponds to the resonant phase velocity of Landau damping. As seen in Fig. 3b, this resonant phase velocity at $r_{\text{eff}}/a_{99} = 0.79$, decreases in time from 230 to 100 km/s and is within 2 ms after the onset of the MHD burst. The decrease in resonant phase velocity is due to the change in the frequency of the exciting wave plotted in Fig. 2b. Since this wave is excited by helically-trapped-energetic-ions through inverse Landau damping, the precession frequency of the helically trapped ions determines the frequency of the exciting wave³¹. Therefore, the frequency decrease of the exciting wave is due to the energy

decrease of helically-trapped-energetic-ions, which contributes to the inverse Landau damping process.

The amplitude of the bipolar velocity-space signature also decreases in time, especially in a velocity regime smaller than the resonant velocity. The wave phase velocity (Methods) is evaluated from the frequency of plasma displacement and the toroidal mode number of magnetic field perturbation. Figure 3c shows the relation between the wave's phase velocity, estimated from the frequency and mode number of the wave measured with the plasma displacement, and resonant phase velocity evaluated from the bipolar velocity-space signature. The relation between wave phase velocity and resonant velocity is nearly linear, with a coefficient of 0.97 ± 0.02 and a correlation coefficient of 0.95 . The bipolar signature of the velocity distribution function at the resonance velocity is evidence of Landau damping. Because several cycles of the wave appear before it damps, the resonance velocity should correlate with the wave phase velocity excited in the case of Landau damping. Therefore, the agreement between phase velocity and resonant velocity is evidence that the wave-particle interaction plays an essential role in the case of Landau damping.

Collisionless energy transfer. There are two processes for causing the decrease of deuterium beam pressure detected with a neutron flux. One is the decrease of effective beam energy due to the collisionless energy transfer from the deuterium beam to bulk ions. The other is the decrease in beam particles due to the redistribution in the radial profile associated with the MHD burst. The collisionless energy transfer can be identified by the simultaneous decrease of stored beam energy and increase of stored bulk ion energy. The decrease of stored beam energy is evaluated from a drop in the neutron flux. The increase of stored carbon energy is evaluated by integrating the energy gain (M_0M_2) over the minor plasma radius (volume integration).

Figure 4a–c shows the radial profiles of 0th, 1st, and 2nd moments of ion velocity distribution before and during the MHD burst. The 0th moment of the ion velocity distribution is almost unchanged during the MHD burst. A change in M_1 is observed in the wider region of the plasma at $r_{\text{eff}}/a_{99} > 0.3$. Because $M_2 \gg M_1^2$, the increment of carbon energy is evaluated from the volume integrated M_0M_2 (in this experiment, M_0 is unchanged even during the MHD burst). In contrast, the 2nd moment M_2 , which is equivalent to the kinetic energy of ions, indicates a significant increase during the MHD burst only at $r_{\text{eff}}/a_{99} > 0.6$. There is no drop in M_2 near the plasma center at $r_{\text{eff}}/a_{99} < 0.6$. It should be noted that the change in velocity distribution function is due to the redistribution in velocity space and is not due to the redistribution in real space. As seen in Fig. 4d, the increase of stored carbon energy is proportional to the decrease of stored beam energy at the onset of the MHD burst (< 0.1 ms), which indicates that the decrease of stored beam energy is mainly due to collisionless energy transfer. In contrast, at the later phase of the MHD burst (> 0.1 ms), there is only a slight increase of stored carbon energy, despite the continuous decrease of stored beam energy, which indicates that this decrease is due to the enhancement of diffusion. Although the carbon impurity concentration is only 1.5% of the bulk ions, the 3 – 6% of beam energy is transferred to the carbon impurity. This fact implies the higher collisionless energy transfer rate of carbon impurity ions rather than bulk ions.

Transit-time damping. Figure 5 shows the expanded view of the magnetic field perturbation and plasma displacement at $r_{\text{eff}}/a_{99} = 0.83$ and skewness (M_3) of ion velocity distribution at $r_{\text{eff}}/a_{99} = 0.79$ for the discharge for transit-time. Both the

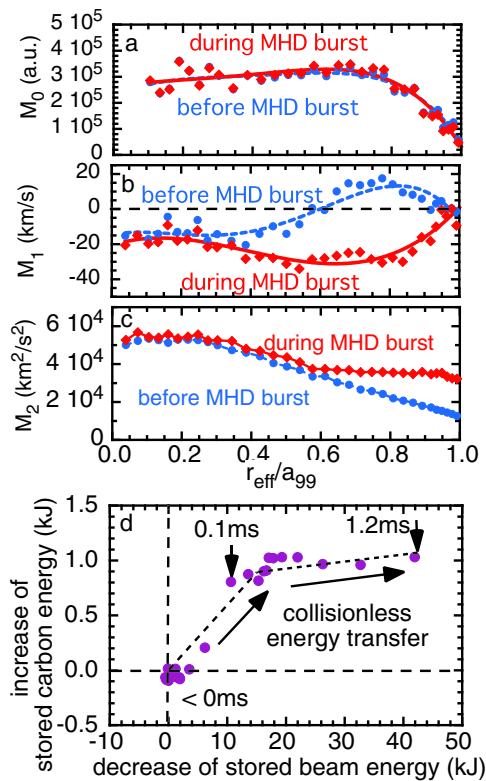


Fig. 4 Collisionless energy transfer to carbon impurity ions. Radial profiles of **a** 0th moment, **b** 1st moment, **c** 2nd moment of ion velocity distribution function of carbon impurity ions before (blue circles and lines) and during MHD (magnetohydrodynamics) burst (red circles and lines) and **d** relation between the increase of stored carbon energy and decrease of stored energy (#164992, #165851, #165859, #165862, #165863, #165943, #165971, #165977).

magnetic field perturbation and the plasma displacement at $r_{\text{eff}}/a_{99} = 0.83$ show a solitary wave feature with only one cycle. There is residual oscillation with small amplitude in the magnetic field perturbation but not in the plasma displacement. The frequency spectrum power, both the magnetic field perturbation and the plasma displacement, shows a strong peak at the jump of RF intensity. The contour of magnetic field perturbation in the space of the toroidal angle indicates that this residual oscillation has a toroidal mode number the same as the discharge with Landau damping. The skewness jumps to 0.2 from zero at the onset of the MHD event and gradually decreases to zero level within 1.5 ms. The decay in skewness value is faster than in the discharge with Landau damping. The time evolution of skewness indicates that the rapid distortion of the ion velocity distribution function from the Maxwell-Boltzmann distribution occurs similarly to the discharge with Landau damping. The distortion of the ion velocity distribution function associated with the solitary wave is evidence of transit-time damping.

Figure 6a–d shows the distribution function of ion velocity and its difference in velocity distribution function before and after the onset of the solitary wave for carbon impurity ions and bulk ions. It should be noted that the deformation of phase velocity at the onset of the solitary wave appears at ~ 210 km/s, both for carbon impurity and bulk ions, although the velocity distribution function of bulk is much broader than that for carbon impurity ions. The zero-cross phase velocity just after the transit-time damping represents the resonant phase velocity. The resonant phase velocity v_{res} normalized by thermal velocity, v_{th} , is 0.4

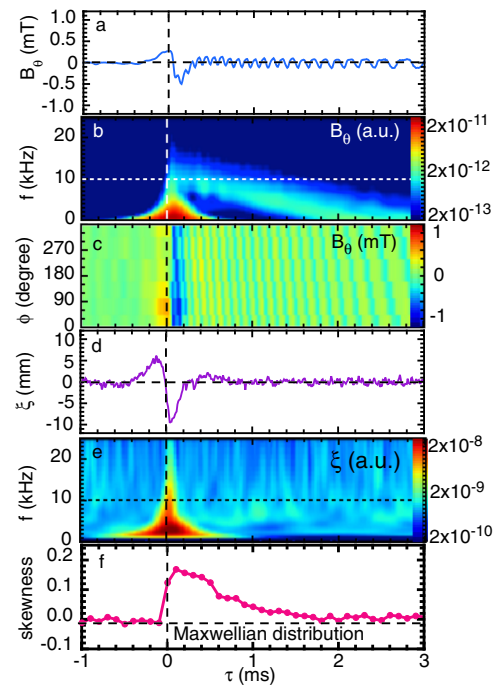


Fig. 5 Characteristics of transit-time damping. Time evolution of **a** magnetic field perturbation, **b** frequency spectrum power of magnetic field perturbation, **c** contour of magnetic field perturbation, **d** plasma displacement at $r_{\text{eff}}/a_{99} = 0.83$ evaluated from perturbation of electron temperature, **e** frequency spectrum power of plasma displacement, and **f** skewness of ion velocity distribution function at $r_{\text{eff}}/a_{99} = 0.79$ with controlled averaging with respect to the collapse time of energetic ions, as indicated by the sharp increase in radio frequency (RF) intensity, plotted in Fig. 1c. (#165933, #165935, #165942, #165944, #165946, #165958, #165964, #165965, #165968, #165979, #165985, #166002, #166008).

($v_{\text{res}}/v_{\text{th}} < 1$) for the bulk ions and 1.1 ($v_{\text{res}}/v_{\text{th}} \sim 1$) for the carbon impurity ions. In the Landau damping and transit-time damping, a larger velocity gradient in the velocity distribution function contributes to the higher energy transfer rate from wave to ions. The resonant velocity normalized by the thermal velocity, which is proportional to the square root of the inverse of atomic mass, is a crucial parameter in the collisionless energy transfer rate.

This is clear evidence that the deformation of velocity distribution, known as a bipolar signature, occurs at the resonance phase velocity, as predicted by Landau and transit-time damping. Although the bipolar velocity-space signature is observed both for bulk and carbon impurity ions, there are significant differences in the time evolution of the zero-cross phase velocity. The zero-cross phase velocity decreases from 220 to 40 km/s in 2 ms in carbon impurity ions. In contrast, only slight decreases of zero-cross phase velocity are observed in bulk ions, as seen in Fig. 6e. Since the solitary wave disappears within 0.2 ms, zero-cross phase velocity decreases due to a relaxation process after the transit-time damping. The relaxation process, characterized by the decrease of zero-cross phase velocity, is fast for carbon impurity ions where the ion-ion collision time scale is 0.8 ms. In contrast, this relaxation process is too slow to be observed within a few ms for the bulk ions, where the ion-ion collision time scale is 12 ms. The energy gain is evaluated by the relative increment of $M_0 M_2$ integrated only in the positive velocity from 0 to $2.5v_{\text{th}}$. Since the $M_0 M_2$ in the negative velocity is almost unchanged, the relative energy gain is defined as $(M_0 M_2(v > 0, \tau > 0) - M_0 M_2(v > 0, \tau < 0))/2M_0 M_2(v > 0, \tau < 0)$.

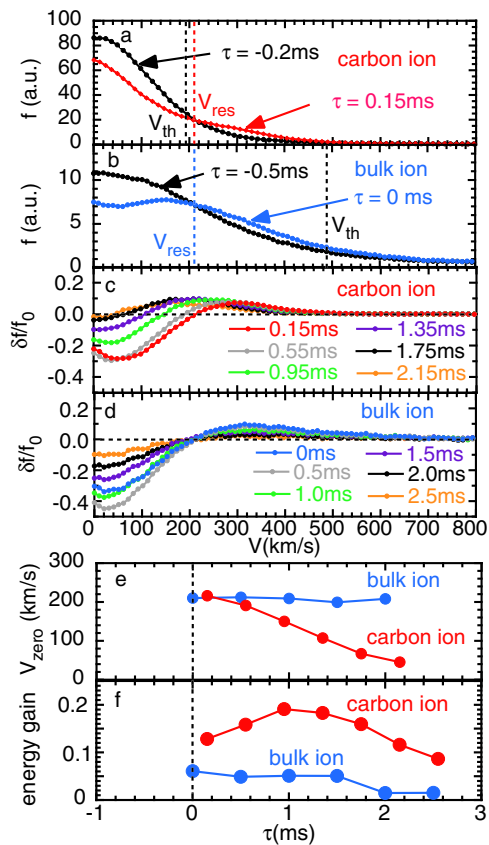


Fig. 6 Energy gain of carbon impurity ions and bulk ions after the transit-time damping. Distribution function of ion velocity at $r_{\text{eff}}/a_{99} = 0.79$, before (black circles and lines) and at the onset of solitary wave (red and blue circles and lines) for **a** carbon impurity ions and for **b** bulk ion and the difference of velocity distribution function before and 0.15 ms (red), 0.55 ms (gray), 0.95 ms (green), 1.35 ms (purple), 1.75 ms (black), 2.15 ms (orange) after the onset of solitary wave for **c** carbon impurity ions and 0 ms (blue), 0.5 ms (gray), 1.0 ms (green), 1.5 ms (purple), 2.0 ms (black), 2.5 ms (orange) after the onset of solitary wave for **d** bulk ions. The time evolution of **e** zero-cross velocity and **f** energy gain (M_2M_0) of bulk ions (blue circles) and carbon impurity ions (red circles). The error bars in **e** and **f** are uncertainties attributed to an evaluation of zero-cross velocity and integration of bipolar signature, respectively, and they are smaller than the symbols. (#175095, #175097, #175104, #175364, #175366).

The energy gain from solitary wave to carbon impurity ions is 2–3 times larger than that of bulk ions, as seen in Fig. 6f. This observation clearly shows that the energy transfer from solitary wave to the particle is higher for the carbon impurity ions with larger atomic mass ($M = 12$) than the bulk ions with smaller atomic mass ($M = 1.75$) (Methods). This mass dependence in collisionless energy transfer rate contrasts with the charge-to-mass ratio dependence in collisional energy transport usually observed in magnetized plasma. The energy transfer from solitary wave to carbon impurity ions is larger than that of bulk ions by approximately the square root of a mass ratio of 7. More observations of energy gain in the wide range of mass ratios are necessary to discuss the detailed mass dependence of energy gain. The mechanism of this mass dependence of energy transfer from a wave to a particle is also a future study. Collisional energy transfers from carbon impurity ions to bulk ions in the ion-ion collision time scale. Therefore, carbon impurity plays a vital role as a mediator in the collisionless energy transfer from energetic ions to bulk ions.

Discussion

In collisionless space and astrophysical plasmas, Landau and transit-time damping are essential processes for energy transfer^{17,40}. The collisionless energy transfer between distinct particle populations through two-way wave-particle energy transfer has been observed in laboratory and space plasma. In the Earth's magnetosphere, the Landau damping is observed for Alfvén waves excited by interplanetary shock⁴¹, whistler-mode waves⁴², and obliquely propagating electromagnetic ion cyclotron (EMIC) waves^{43,44}. Theoretical studies suggest that both electrons and ions interact with obliquely propagating EMIC waves through Landau resonance^{43,45}. Electron heating by EMIC waves inside the plasmaspheric plume has been reported and explained by the Landau damping of EMIC waves⁴⁴. The energy transfer via wave-particle interaction can occur both at the Landau and cyclotron resonance. The energy transfer from hot protons to cold Helium through the cyclotron resonance between an EMIC wave and ions has been directly confirmed in the Earth's magnetosphere^{46–48}. The collisionless energy transfer between different species is a crucial issue in understanding the energy balance between species in plasma, regardless of the resonance process. In this experiment, the energy transfer from trapped energetic ions to thermalized ions was higher for the species with heavier mass. The mass dependence of energy transfer from wave to the particle is crucial to evaluate the energy balance in multi-species collisionless plasma. Therefore, the mass-dependent collisionless energy transfer observed in this experiment gives new insight into understanding the acceleration of ions with different mass, through the interaction between the particle and chirping wave or solitary wave in space and astrophysical plasmas as well as in magnetically confined plasma.

Methods

Large Helical Device: experimental device. The Large Helical Device (LHD) is a heliotron type device for the magnetic confinement of high-temperature plasmas with a magnetic field, B , of 2.75 T at the magnetic axis in the vacuum field, major, R_{ax} , and effective minor radius r_{eff} , of 3.6 m and 60–65 cm, respectively. The LHD is equipped with five neutral beams (NBs), and three of them are injected in the direction parallel to the magnetic field, and two are injected perpendicular to the magnetic field. The central electron and ion temperatures are 4 and 6 keV, respectively, and the central electron density is $1 \times 10^{19} \text{ m}^{-3}$. In this experiment, the beam species of three parallel NBs are hydrogen, the beam species of two perpendicular NBs are deuterium, and neutrons are mainly created by the reaction between the perpendicular beams and plasma. The fraction of hydrogen and deuterium ions is measured by spectroscopy. The bulk ions are mainly deuterium, but the parallel beams cause hydrogen contamination (~25%). Therefore, the average mass of a bulk ion is 1.75. Therefore, the amount of trapped energetic ions injected by perpendicular deuterium NBs is monitored by the neutron flux, measured with a scintillation detector³⁰. The RF intensity measured with an RF radiation probe³² is widely used as a timing indicator for the energetic ion loss from the plasma. The jump of RF intensity measured with 880 MHz at a toroidal angle of $\phi = 121^\circ$ is used for conditional averaging as a reference time for the onset of the MHD burst. Charge exchange spectroscopy³⁵ is used to measure ion velocity distribution along the line of sight. There are two lines of sight, one is parallel to the magnetic field, and the other is perpendicular to the magnetic field. The magnetic probes are installed inside the vacuum vessel at toroidal angles of 18° , 90° , 126° , 198° , 270° , and 342° . The intensity of the electron cyclotron emission (ECE)³⁶ is proportional to the plasma electron temperature, T_e . The ECE diagnostic is located at a toroidal angle of 198° . Because the plasma electron temperature is constant on a magnetic field line, the perturbation of the equi-temperature plasma surface is equivalent to the perturbation of the magnetic flux surface. Therefore, the perturbation of the magnetic field inside the plasma can be measured from the displacement of the equi-temperature plasma surface as $-\delta T_e / \nabla T_e$, where δT_e is the temperature fluctuation in the frequency range of 1–10 kHz and ∇T_e is the quasi-state (<40 Hz) temperature gradient.

Beam pressure evaluated from neutron flux. We estimate the amount of stored beam energy by measuring the neutron emission rate from the D-D reaction. Although the thermal-thermal fusion reaction could be dominant in tokamaks, the beam-thermal reaction is dominant in LHD plasmas. In the experiment, the neutron rate does not depend much on the density and temperature of bulk ions but strongly depends on the stored deuterium beam energy. The neutron emission rate S_n is proportional to the product of the number of beam ions (n) and cross-

section $\langle \sigma v \rangle$, which strongly depends on the beam velocity (v). The beam energy can be expressed as $(1/2)mv^2$, where m is beam mass. The relation between beam energy E_{mbi} [$= (1/2)mv^2$] and neutron emission rate S_n is calculated using the simulation code, TASK/FP³¹. Neutrons are mainly created by the reaction between perpendicular beams and plasma. Therefore, the drop in the neutron emission rate indicates a change in beam energy E_{mbi} , due to the inverse Landau damping and a change (enhancement) in beam ion losses. The decrease of stored beam energy is evaluated from a decrease in the neutron emission rate, using the relation between the emission rate and beam energy, calculated by the simulation code TASK/FP.

Fast charge exchange spectroscopy. In high-temperature plasmas, the spectral lines have broadened due to the Doppler effect caused by a distribution of velocities of ions. In laboratory plasma, charge exchange spectroscopy is commonly used to measure the local ion temperature and flow velocity by fitting the velocity distribution function, f , to a Gaussian profile. The charge exchange spectroscopy provides a local measurement at the intersection between the line of sight and the line of neutral beam injected. The intensity of the spectrum is simply proportional to the number of ions with the velocity corresponding to the Doppler shift, and this spectroscopy gives a local velocity distribution function in plasmas. In this experiment, charge exchange spectroscopy is used to measure the distortion of velocity distribution function δf from Maxwell-Boltzmann distribution (Gaussian profile). In a steady-state condition, the velocity distribution function is Maxwell-Boltzmann distribution, due to thermalization through ion-ion collision. Therefore, the time resolution of velocity distribution function measurements should be shorter than the ion-ion collision time scale ($\sim 10^{-3}$ sec for carbon impurity ions and $\sim 10^{-2}$ sec for deuterium ions in this plasma). The fast charge exchange spectroscopy developed for this experiment consists of a high throughput spectrometer with lens, image intensifier, and fast camera and provides the local velocity distribution at a frequency of 10 kHz for carbon impurity ions and 2 kHz for bulk ions. The integration time for the ion velocity distribution function measurements is 0.1 ms for carbon impurity ions and 0.5 ms for bulk ions. The pixel resolution of the velocity measurements is 12 km/s for carbon impurity ions and 10 km/s for bulk ions.

MHD burst. The modes excited by the MHD instability can be categorized as low-frequency shear Alfvén eigenmodes mode-driven energetic ions.⁴⁹ Although the parallel electric field to the magnetic field is zero in the ideal MHD, the energy transfer between charged particles and Alfvén eigenmodes take place through the magnetic (grad-B and curvature) drifts and the perpendicular electric field²⁰. Although it is not easy to identify the unstable modes in the toroidal plasma because of the complexity of three-dimensional geometry, the characteristics of the unstable mode are clarified in the experiment. The MHD burst is triggered by the collapse of a tongue-shaped deformation, which occurs not at the resonant magnetic flux surface, the so-called rational surface, but at the off-resonant magnetic flux surface^{27–29}. The tongue deformation is radially, poloidally, and toroidally localized and cannot be expressed with a mode number, which is usually used in the simulation. After the collapse of the tongue-shaped deformation, the MHD burst with the $n/m = 1/1$ mode starts to rotate toroidally with a frequency of ~ 10 kHz. Here n and m are toroidal and poloidal mode numbers, respectively. The pre-cursor wave mode before the main event (collapse of a tongue-shaped deformation) has an $n/m = 1/1$ mode number and interchange parity in radius (even parity: in-phase across the rational surface). It is identical both for Landau and transit-time damping cases. In contrast, after the main event, the post-cursor wave mode has the $n/m = 1/1$ mode number but tearing parity in radius (odd parity: out-of-phase across the rational surface)²⁸. This post-cursor wave mode is much weaker than the solitary wave excited by the collapse of tongue-shaped deformation in the case of transit-time damping. In contrast, this post-cursor wave mode is stronger than the solitary wave in the case of Landau damping. Because of the difficulty of including this trigger mechanism in the simulation, no theoretical and numerical work can derive reasonable expectations of power transferred from energetic ions to impurity ions.

Estimate of resonant and wave phase velocity. In the Landau damping process, the particles initially moving at velocities slightly slower than the phase velocity of the wave gain energy from the wave, while the particles initially moving at velocities slightly faster than the phase velocity, lose energy to the wave. Because the number of particles with velocities smaller than the wave phase velocity is greater than those with velocities larger than the wave phase velocity in the Maxwell-Boltzmann distribution, this process results in the decay of the wave amplitude and the increase of kinetic energy of particles. The increase of the kinetic energy of a particle can be observed with the bipolar signature of the ion velocity distribution function, where the simultaneous increase/decrease of the ion population with the phase velocity larger/smaller than the resonant velocity appears. The resonant phase velocity of Landau damping is evaluated from the zero crossings velocity in the bipolar signature, observed in the ion velocity distribution, measured with fast charge exchange spectroscopy. The phase velocity of the wave ω/k_{\parallel} is evaluated from the oscillation frequency, $f = \omega/(2\pi)$, and the wavenumber, $k_{\parallel} = n/R$, where R is the major radius and n is the toroidal mode. Because the ECE diagnostic is installed only at one toroidal location ($\phi = 198^\circ$), the toroidal mode number of the MHD burst cannot be evaluated from the ECE measurement. The estimate of the toroidal mode number requires diagnostics with an array distributed in the toroidal

direction. The toroidal mode number is evaluated from the phase shift of the toroidal magnetic probe array. The magnetic field perturbations at 90° and 270° are out of phase, which indicates that the toroidal mode number is odd. The contour of the power in time and toroidal angle clearly shows that the toroidal mode number $n = 1$. The major radius R , where the wave is excited, is 4.25 m. The frequency of the magnetic field perturbation and the phase velocity decrease from 9 to 2 kHz and from 230 to 50 km/s, respectively, within 2 ms.

Moment analysis of ion velocity distribution function. The distortion of ion velocity distributions from the Maxwell-Boltzmann distribution is evaluated quantitatively, using moment analysis of the ion velocity distribution function. The moment analysis is a valuable tool to evaluate the contribution of the non-Maxwell component of the velocity distribution function. The 0th, 1st, 2nd, and 3rd moments of the ion velocity distributions are defined as

$$M_0 = \int f(v)dv, \quad (1)$$

$$M_1 = \frac{1}{M_0} \int vf(v)dv, \quad (2)$$

$$M_2 = \frac{1}{M_0} \int (v - M_1)^2 f(v)dv, \quad (3)$$

$$M_3 = \frac{1}{M_0 M_2^{3/2}} \int (v - M_1)^3 f(v)dv. \quad (4)$$

Here, M_0 corresponds to the number density of the species. When the velocity function $f(v)$ is Maxwell-Boltzmann distribution, each moment becomes $M_1 = V_s$, $M_2 = V_{th}^2/2 = T_i/m_i$, $M_3 = 0$, where V_s is the projection of the flow velocity to the line-of-sight, V_{th} is thermal velocity, T_i is the ion temperature, and m_i is the ion mass. The 3rd moment, M_3 , the so-called skewness, is a good measure for the asymmetric distortion of velocity distribution from Maxwell-Boltzmann distribution in the Landau damping. In this experiment, the moment of ion velocity distribution is evaluated up to 4. A moment as high as five is not detectable in this experiment. Before the onset of the MHD event, the 3rd moment, M_3 , (skewness), is zero, and the 3rd moment, M_4 , (kurtosis), is three within the error bars, showing that the ion velocity distribution is nearly Maxwellian thermal velocity distribution. When the skewness becomes non-zero, the value of the ion temperature, T_i , cannot be determined by Gaussian fitting of the spectrum in velocity space. Therefore, the product of M_0 and M_2 is used as a measure of the energy of carbon impurity ions and bulk ions.

Conditional averaging technique. The precise measurements of the ion distribution function, especially distortion from Maxwell-Boltzmann distribution, require a high signal-to-noise ratio (S/N). On the other hand, a high time resolution is also required for this study because of the rapid change in velocity distribution by the MHD burst. Because the S/N is always a trade-off of the time resolution of the measurements, conditional averaging is a powerful tool to improve S/N in the measurement, especially for a repeated event such as the MHD burst. The conditional averaging for an arbitrary time-dependent function $\Psi(t, \dots)$ is defined as

$$\bar{\Psi}(\tau, \dots) = \frac{1}{N} \sum_{i=1}^N \Psi(t_i + \tau, \dots) \quad (5)$$

where the value t_i indicates the i th time where trigger events occur, N is the total number of events, and τ is the relative time with respect to the sharp increase of the RF intensity. In the present application, $\Psi(t, \dots)$ is either $B_\theta(t)$, $\xi(t)$, or $f(t, v)$. Conditionally averaged signals $\bar{B}_\theta(t)$ and $\bar{\xi}(t)$ are then decomposed in the time-frequency space by Morlet wavelet analysis. Moments of conditionally averaged velocity distribution function $\bar{f}(t, v)$ are also calculated according to Eqs. (1)–(4) above. All of the MHD burst events with similar discharge (~ 10 shots) are accumulated for the conditional averaging in this study.

Data availability

The datasets generated during and/or analyzed during the current study are available in the Large Helical Device (LHD) data repository server of the National Institute for Fusion Science (NIFS) at https://www-lhd.nifs.ac.jp/pub/Repository_en.html.

Received: 21 April 2022; Accepted: 30 August 2022;

Published online: 28 September 2022

References

- Landau, L. D. On the vibrations of the electronic plasma. *J. Phys. (Moscow)* **10**, 25 (1946).

2. Dawson, J. On Landau damping. *Phys. Fluids* **4**, 869–874 (1961).
3. Robinson, P. A. New contributions to transit-time damping in multidimensional systems. *Phys. Fluids B* **1**, 490–498 (1989).
4. Robinson, P. A. Transit-time damping and the arrest of wave collapse. *Phys. Fluids B* **3**, 545–554 (1991).
5. Melatos, A. & Robinson, P. A. Transit-time interactions in magnetized plasmas. *Phys. Fluids B* **5**, 1045–1056 (1993).
6. Short, R. W. & Simon, A. Landau damping and transit-time damping of localized plasma waves in general geometries. *Phys. Plasmas* **5**, 4124–4133 (1998).
7. Skjæraasen, O., Robinson, P. A. & Melatos, A. Local transit-time dissipation and Landau damping. *Phys. Plasmas* **6**, 3435–3441 (1999).
8. Wong, A. Y., Motley, R. W. & D'Angelo, N. Landau damping of ion acoustic waves in highly ionized plasmas. *Phys. Rev.* **133**, A436–A442 (1964).
9. Malmberg, J. H. & Wharton, C. B. Dispersion of electron plasma waves. *Phys. Rev. Lett.* **17**, 175–178 (1966).
10. Chang, R. P. H. & Porkilab, M. Experimental observation of nonlinear Landau damping of plasma waves in a magnetic field. *Phys. Rev. Lett.* **25**, 1262–1266 (1970).
11. Gentle, K. W. & Maleint, A. Observations of nonlinear Landau damping. *Phys. Rev. Lett.* **26**, 625–628 (1971).
12. Ikezi, H. Experiments on ion-acoustic solitary wave. *Phys. Fluids* **16**, 1668–1675 (1973).
13. Schroeder, J. W. R. Laboratory measurements of the physics of auroral electron acceleration by Alfvén waves. *Nat. Commun.* **12**, 740 (2021).
14. Medvedev, M. V., Diamond, P. H., Rosenbluth, M. N. & Shevchenko, V. I. Asymptotic theory of nonlinear Landau damping and particle trapping in waves of finite amplitude. *Phys. Rev. Lett.* **81**, 5824–5827 (1998).
15. Prakash, M. & Diamond, P. H. The role of nonlinear Landau damping and the bounced motion of protons in the formation of dissipative structures in the solar wind plasma. *Nonlin. Processes Geophys.* **6**, 161–167 (1999).
16. Howes, G. G. A prospectus on kinetic heliophysics. *Phys. Plasmas* **24**, 055907 (2017).
17. Chen, C. H. K., Klein, K. G. & Howes, G. G. Evidence for electron Landau damping in space plasma turbulence. *Nat. Commun.* **10**, 740 (2019).
18. Horvath, S. A., Howes, G. G. & McCubbin, A. J. Electron Landau damping of kinetic Alfvén waves in simulated magnetosheath turbulence. *Phys. Plasmas* **27**, 102901 (2020).
19. Howes, G. G. Laboratory space physics: Investigating the physics of space plasmas in the laboratory. *Phys. Plasmas* **25**, 055501 (2018).
20. Todo, Y. Introduction to the interaction between energetic particles and Alfvén eigenmodes in toroidal plasmas. *Rev. Mod. Plasma Phys.* **3**, 1 (2019).
21. Howes, G. G., McCubbin, A. J. & Klein, K. G. Spatially localized particle energization by strong Alfvén wave collisions. *J. Plasmas Phys.* **84**, 905840105 (2018).
22. Wang, H., Todo, Y., Ido, T. & Suzuki, Y. Chirping and sudden excitation of energetic-particle-driven geodesic acoustic modes in a large helical device experiment. *Phys. Rev. Lett.* **120**, 175001 (2018).
23. Wang, H., Osakabe, M., Todo, Y., Ido, T. & Suzuki, Y. Simulation of energetic particle driven geodesic acoustic modes and the energy channeling in the Large Helical Device plasmas. *Nucl. Fusion* **59**, 096041 (2019).
24. Todo, Y., Sato, M., Wang, H., Ido, T., Seki, R. Magnetohydrodynamic hybrid simulation model with kinetic thermal ions and energetic particles. *Plasma Phys. Control. Fusion* **63**, 075018 (2021).
25. Du, X. D. Resistive interchange modes destabilized by helically trapped energetic ions in a helical plasma. *Phys. Rev. Lett.* **114**, 155003 (2015).
26. Ida, K. Abrupt onset of tongue deformation and phase space response of ions in magnetically-confined plasmas. *Sci. Rep.* **6**, 36217 (2016).
27. Ida, K. Observation of distorted Maxwell-Boltzmann distribution of epithermal ions in LHD. *Phys. Plasmas* **24**, 122502 (2017).
28. Ida, K. Trigger mechanism for the abrupt loss of energetic ions in magnetically confined plasmas. *Sci. Rep.* **8**, 2804 (2018).
29. Voermans, S. Characteristics of tongue-shaped deformations in hydrogen and deuterium plasmas in the Large Helical Device. *Nucl. Fusion* **59**, 106041 (2019).
30. Ogawa, K. Energetic particle transport and loss induced by helically-trapped energetic-ion-driven resistive interchange modes in the Large Helical Device. *Nucl. Fusion* **60**, 112011 (2020).
31. Bando, T. Excitation of helically-trapped-energetic-ion driven resistive interchange modes with intense deuterium beam injection and enhanced effect on beam ions/bulk plasmas of LHD. *Nucl. Fusion* **58**, 082025 (2018).
32. Sakakibara, S. Magnetic measurements in LHD. *Fusion Sci. Technol.* **58**, 471–481 (2010).
33. Ogawa, K., Isobe, M., Kawase, H. & Nishitani, T. Neutron flux measurement using a fast-neutron scintillation detector with high temporal resolution on the large helical device. *Plasma Fusion Res.* **13**, 3402068 (2018).
34. Nuga, H. Analysis of beam slowing-down process in Large Helical Device based on Fokker-Planck operator including beam-beam Coulomb collision effect. *Nucl. Fusion* **59**, 016007 (2019).
35. Leem, J., Yun, G. S. & Park, H. K. Development of fast RF spectrometer system for MHD detection. *J. Instrum.* **7**, C01042 (2012).
36. Heidbrink, W. W. Characterization of off-axis fishbones. *Plasma Phys. Control. Fusion* **53**, 085028 (2011).
37. Du, X. D. Suppression of trapped energetic ions driven resistive interchange modes with electron cyclotron heating in a helical plasma. *Phys. Rev. Lett.* **118**, 125001 (2017).
38. Yoshinuma, M., Ida, K., Yokoyama, M., Osakabe, M. & Nagaoka, K. Charge-exchange spectroscopy with pitch-controlled double-slit fiber bundle on LHD. *Fusion Sci. Technol.* **58**, 375–382 (2010).
39. Tokuzawa, T. Developments of electron cyclotron emission spectroscopy and microwave reflectometry on LHD. *Fusion Sci. Technol.* **58**, 364–374 (2010).
40. Miyoshi, Y. Penetration of MeV electrons into the mesosphere accompanying pulsating aurorae. *Sci. Rep.* **11**, 13724 (2021).
41. Wang, C., Rankin, R. & Zong, Q. Fast damping of ultralow frequency waves excited by interplanetary shocks in the magnetosphere. *J. Geophys. Res. Space Phys.* **120**, 2438–2451 (2015).
42. Bell, T. F., Inan, U. S., Bortnik, J. & Scudder, J. D. The Landau damping of magnetospherically reflected whistlers within the plasmasphere. *Geophys. Res. Lett.* **29**, 1733 (2002).
43. Thorne, R. M. & Horne, R. B. The contribution of ion-cyclotron waves to electron heating and SAR-arc excitation near rhw storm-time plasmopause. *Geophys. Res. Lett.* **19**, 417–420 (1992).
44. Yuan, Z. Cold electron heating by EMIC waves in the plasmaspheric plume with observations of the Cluster satellite. *Geophys. Res. Lett.* **41**, 1830–1837 (2014).
45. Horne, R. B. & Thorne, R. M. Wave heating of He⁺ by electromagnetic ion cyclotron waves in the magnetosphere: Heating near the H⁺-He⁺ bi-ion resonance frequency. *J. Geophys. Res.* **102**, 11457–11471 (1997).
46. Kitamura, N. Direct measurements of two-way wave-particle energy transfer in a collisionless space plasma. *Science* **361**, 1000 (2018).
47. Shoji, M. Discovery of proton hill in the phase space during interactions between ions and electromagnetic ion cyclotron waves. *Sci. Rep.* **11**, 13480 (2021).
48. Nakamura, S., Omura, Y., Kletzing, C. & Baker, D. N. Rapid precipitation of relativistic electron by EMIC rising-tone emissions observed by the Van Allen probes. *J. Geophys. Res. Space Phys.* **124**, 6701–6714 (2019).
49. Heidbrink, W. W. Basic physics of Alfvén instabilities driven by energetic particles in toroidally confined plasma. *Phys. Plasmas* **15**, 055501 (2008).

Acknowledgements

We wish to thank the LHD experiment group for the excellent support of this work. This work is supported by Grants-in-Aid for Scientific Research (21H04973 to K.I.; 21K13902 to T.K.; 19K03798 to K.O.; 19H01880 to T.T.; and 18H03727 to Y.K.) of the Japan Society for the Promotion of Science (JSPS).

Author contributions

K.I. conceived and designed the study, found this event from the data, analyzed the data, and wrote the initial draft. T.K. contributed to the moment analysis and conditioning averaging of ion velocity distribution function, plasma displacement, and magnetic field perturbation. M.Y. contributed to the development of fast charge exchange spectroscopy for deriving the distribution function of ion velocity. K.N. and Y.K. contributed to the interpretation of the result. K.O. contributed to developing magnetic probes for magnetic field perturbation measurement and a scintillation detector for neutron flux measurement. H.N. contributed to evaluating stored beam energy from neutron flux using the simulation code. T.T. contributed to the development of electron cyclotron emission (ECE) for the measurement of plasma displacement.

Competing interests

The authors declare no competing interests.

Additional information

Supplementary information The online version contains supplementary material available at <https://doi.org/10.1038/s42005-022-01008-9>.

Correspondence and requests for materials should be addressed to Katsumi Ida.

Peer review information *Communications Physics* thanks the anonymous reviewers for their contribution to the peer review of this work. Peer reviewer reports are available.

Reprints and permission information is available at <http://www.nature.com/reprints>

Publisher's note Springer Nature remains neutral with regard to jurisdictional claims in published maps and institutional affiliations.



Open Access This article is licensed under a Creative Commons Attribution 4.0 International License, which permits use, sharing, adaptation, distribution and reproduction in any medium or format, as long as you give appropriate credit to the original author(s) and the source, provide a link to the Creative Commons license, and indicate if changes were made. The images or other third party material in this article are included in the article's Creative Commons license, unless indicated otherwise in a credit line to the material. If material is not included in the article's Creative Commons license and your intended use is not permitted by statutory regulation or exceeds the permitted use, you will need to obtain permission directly from the copyright holder. To view a copy of this license, visit <http://creativecommons.org/licenses/by/4.0/>.

© The Author(s) 2022